Cap plasticity models and compactive and dilatant pre-failure deformation

A. F. Fossum and J. T. Fredrich
Sandia National Laboratories, Albuquerque, New Mexico

ABSTRACT: At low mean stresses, porous geomaterials fail by shear localization, and at higher mean stresses, they undergo strain-hardening behavior. Cap plasticity models attempt to model this behavior using a pressure-dependent shear yield and/or shear limit-state envelope with a hardening or hardening/softening elliptical end cap to define pore collapse. While these traditional models describe compactive yield and ultimate shear failure, difficulties arise when the behavior involves a transition from compactive to dilatant deformation that occurs before the shear failure or limit-state shear stress is reached. In this work, a continuous surface cap plasticity model is used to predict compactive and dilatant pre-failure deformation. During loading the stress point can pass freely through the critical state point separating compactive from dilatant deformation. The predicted volumetric strain goes from compactive to dilatant without the use of a non-associated flow rule. The new model is stable in that Drucker's stability postulates are satisfied.

1 INTRODUCTION

Massively parallel solution algorithms together with newly introduced teraflops supercomputers provide the geoscientist with unprecedented capabilities to simulate the large-scale mechanical behavior of complex geosystems. Along with advances in software and hardware, accurate representations of the nonlinear stress-strain behavior of rock and soil play a critical role in the ability of simulations to predict the natural behavior of geosystems.

Two classes of behavior may be identified on the basis of rock porosity for the range of mean stresses encountered in several geosystems of current engineering interest (e.g. oil and gas reservoirs, nuclear waste repositories, buried targets, and depleted reservoirs for possible use for subsurface sequestration of greenhouse gases). Low porosity rocks exhibit shear localization. High porosity rocks exhibit more varied deformation behavior, including both shear localization and compaction, depending on the mean stress. Cap plasticity models (e.g. DiMaggio & Sandler 1971) attempt to model this behavior using a pressure-dependent shear yield and/or shear limit-state envelope with a hardening or hardening/softening elliptical end cap to define pore collapse.

While the traditional cap plasticity models describe compactive yield and ultimate shear failure, difficulties arise when the rock behavior involves a transition from compactive to dilatant deformation that occurs well before the shear failure or limit-state shear stress is reached. Laboratory rock mechanics tests on porous sandstones and carbonates reveal precisely this behavior. In this paper we describe a continuous surface cap plasticity model that is used to predict both compactive and dilatant pre-failure deformation. During loading the stress point can pass freely through the critical state point separating compactive from dilatant deformation so that the predicted volumetric strain goes from compactive to dilatant without the use of a non-associated flow rule. The new model is stable in that Drucker's stability postulates are satisfied.

2 ROCK MECHANICAL BEHAVIOR

The deformation and failure behavior of rocks involves a complex interplay of multiple inelastic processes that operate at the grain scale. Shear localization results from the growth, interaction and coalescence of microcracks, and inelastic pore collapse is an important yield mechanism in porous sedimentary rocks. Mechanisms for inelastic crack propagation include sliding along pre-existing cracks, elastic mismatch at grain boundaries, point loading, and stress concentrations at pores and twin terminations. Inelastic pore collapse can be accom-

DISCLAIMER

modated by grain rotation, brittle microcracking, and plastic flow (crystalline plasticity and twinning).

Depending on the particular load path that is followed, low-porosity rocks deform elastically under deviatoric compressive loading until a critical stress is reached that is associated with the onset of dilatant microcrack growth (Brace et al. 1966). Loading under a uniaxial strain path thus traces a yield surface that is associated with the onset of dilatancy. For loading under a conventional triaxial compression stress path that crosses the dilatancy yield surface, failure is associated ultimately with the attainment of a peak stress and work-softening deformation. Tensile or extensile microcrack growth dominates the micromechanical processes that result in macroscopically dilatant volumetric strains. Senseny, Fossum, & Pfeifle (1983) presented constitutive models for this general class of behavior in which non-associated flow rules predict accurately pre-failure dilatant strains.

The deformation behavior of high porosity rocks is more varied and depends on the mean stress and load path. At low mean stresses, porous rocks can fail by shear localization and exhibit work-softening behavior; the microscale deformation includes dilatant microcracking and also may include grain rotation. At higher mean stresses, porous rocks undergo strain-hardening behavior associated with macroscopically compactive volumetric strain. Inelastic compaction of the pore space, accommodated by breakage and/or slippage of grain contacts and brittle microcracking, dominates the microscale processes. Depending on the load path that is followed, the material may fail ultimately by shear localization. Cap plasticity models capture this range in behavior.

2.1 *Traditional cap plasticity model*

The constitutive equations referred to as cap plasticity models have been in existence for at least 40 years (Drucker et al. 1957). Traditionally, these models comprise two independent continuously differentiable yield functions. The inner envelope of the two surfaces corresponding to the two smooth yield functions generates the yield surface that defines the boundary of the elastic region. Corners appear at the intersections of the two yield surfaces. In the case of flow, some workers accept that the plastic strain increment is not specified uniquely but is only required to lie between the normals to the yield surface at adjacent points on the yield surface. Other workers attempt to eliminate this indeterminacy by introducing a third yield function that serves to connect the first two yield surfaces continuously. In the case of hardening behavior, the plastic strain increment comprises the sum of the plastic strain increments determined independently from each of the

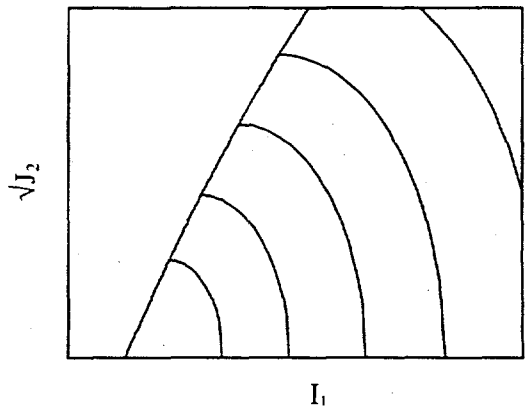

Figure 1. Shear yield surfaces and hardening cap surfaces of the traditional cap plasticity model.

yield functions. The inner envelope of the surfaces must be convex requiring that each individual surface be convex.

The following describes a traditional cap plasticity model (Sandler & Rubin 1979) that is representative of two-surface models. The model is formulated in terms of two invariants, I_1, the first invariant of the Cauchy stress, and J_2, the second invariant of the deviator stress. In terms of principal stresses these invariants are given by

$$I_1 = \sigma_1 + \sigma_2 + \sigma_3 \tag{1}$$

$$J_2 = \frac{1}{6}\left\{(\sigma_1 - \sigma_3)^2 + (\sigma_1 - \sigma_2)^2 + (\sigma_2 - \sigma_3)^2\right\} \tag{2}$$

where $\sigma_1 \geq \sigma_2 \geq \sigma_3$ and compression is taken as negative. If the strength in extension is less than that in compression, as is sometimes observed for rock and other brittle materials such as concrete, a three-invariant model is generally required.

The model can be used to represent elastic behavior, shear failure, and cap plasticity. The model is a classical rate-independent, associative plasticity model in which the yield surface comprises a shear yield surface and a cap that hardens (Fig. 1). The shear yield surface is often fixed (as is shown in Fig. 1), but this is not a model restriction. When this surface is fixed it is usually fitted to shear-failure data and called a shear-failure surface. Elastic behavior occurs when the stress point is within the composite shear-failure and yield-cap surfaces.

When the stress point lies on the shear-failure envelope, shear failure occurs according to the shear-failure function,

$$F_s = \sqrt{J_2} - A + C\exp(BI_1) \tag{3}$$

where A, B, and C are shear-failure parameters. During shear failure, the plastic strain comprises a shear component and a dilatant component.

When the stress point lies on the cap and pushes it outward, plastic strain comprises an irreversible decease in volume called compaction, and a shear component for non-hydrostatic compressive stress

states. The cap motion is related to the plastic decrease in volume through a hardening rule. The shape of the cap is described as an elliptical surface defined by

$$\sqrt{J_2} = \frac{1}{R}\sqrt{(X-L)^2 - (I_1 - L)^2} \tag{4}$$

in which

$$L(\kappa) = \begin{cases} \kappa \ if \ \kappa < 0 \\ 0 \ if \ \kappa \geq 0 \end{cases} \tag{5}$$

$$X = L - R[A - C\exp(BL)] \tag{6}$$

The cap position parameters L and X locate the current cap surface. The material parameter, R, defines the ratio of principal ellipse radii of the cap surface. The hardening parameter, κ, is defined through a functional of $X(\kappa)$ and volumetric plastic strain, ε_v^p, caused only by cap action,

$$\bar{\varepsilon}_v^p = W\left|\exp\left\{D_1(X - X_0) - D_2(X - X_0)^2\right\} - 1\right| \tag{7}$$

in which W, D_1, and D_2 are material parameters, X_0 is the initial cap position, and $\bar{\varepsilon}_v^p$ is a history-dependent functional of ε_v^p given by

$$\dot{\bar{\varepsilon}}_v^p \equiv \min\left(\dot{\varepsilon}_v^p, 0\right) \tag{8}$$

The hydrostatic-pressure/volumetric-strain relationship (Eq. 7), can capture a wide range of compaction behavior including one or two inflection points (Fig. 2).

The cap surface is required to intersect the shear-failure surface at the point of horizontal tangency to the cap ellipse. Thus, the shear-failure surface represents the critical-state line separating dilatant from compactive inelastic volumetric deformation.

The model as discussed has a number of shortcomings. It has already been mentioned that there is an indeterminacy of flow direction at the intersection of the shear-failure surface and the cap-hardening surface. From a numerical standpoint, it is often found that an excessive amount of solution time is spent iterating to find the intersection of the shear-failure surface with the cap-hardening surface. From a physical viewpoint, the requirement that the cap-hardening surface intersect the shear-failure surface at the point of horizontal tangency to the cap ellipse prevents pre-failure dilatant deformation, contradicting experimental observations. Also, it was noted earlier that a three-invariant model is often required for rocks and similar brittle materials.

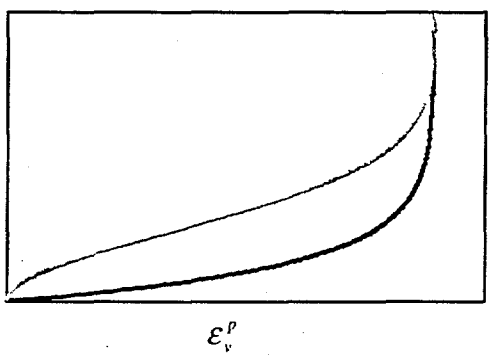

Figure 2. Compaction behavior with one (black) and two (gray) inflection points.

3 CONTINUOUS SURFACE CAP PLASTICITY MODEL

To circumvent the shortcomings of the model described in the previous section, a variation of a technique described by Schwer & Murray (1994) is used to smooth the intersection of the failure and cap-hardening surfaces using a Pelessone function (Pelessone 1989). The resulting continuous, single-surface yield function incorporates shear kinematic hardening, cap isotropic hardening, Lode angle dependence of yield, and is sufficiently general to predict pre-failure dilatant deformation.

The single-surface continuous yield function is given by

$$f\left(I_1, J_2, J_3, \kappa, \alpha_{ij}\right) = \Gamma^2(\beta)\left(J_2 - J_2^{\alpha}\right) - (F_s - N)^2 F_c \tag{9}$$

where κ is the cap-hardening parameter defined by Eq. 5; α_{ij} is the back-stress tensor; Γ is a function of the Lode-angle given by

$$\Gamma = \frac{1}{2}\left\{\left[1 + \sin(3\beta)\right] + \frac{1}{\Psi}\left[1 - \sin(3\beta)\right]\right\} \tag{10}$$

where Ψ is the ratio of the yield stress in triaxial extension to the yield stress in triaxial compression; β is the Lode angle given by

$$\beta = \frac{1}{3}\text{asin}\left(-\frac{27}{2}\frac{J_3}{(3J_2)^{3/2}}\right) \quad -\frac{\pi}{6} \leq \beta \leq \frac{\pi}{6}; \tag{11}$$

J_3 is the third invariant (determinant) of the deviator stress and, J_2^{α}, is the scalar back stress measure given by

$$J_2^{\alpha} = \alpha_{ij}\left(s_{ij} - \frac{\alpha_{ij}}{2}\right). \tag{12}$$

F_s is the shear-failure function defined by Eq. 3; N is a constant defining the size of the initial shear yield surface; and F_c is the non-dimensional Pelessone function given by

$$F_c(I_1, \kappa) = 1 + \frac{(I_1 - L)\left\{|I_1 - L| - (I_1 - L)\right\}}{2(X - L)^2} \tag{13}$$

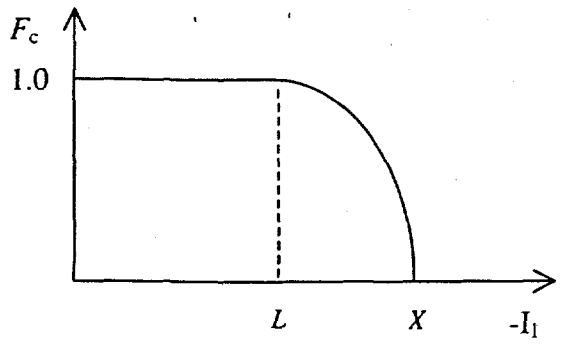

Figure 3. Non-dimensional function for the cap component of the single-surface cap model.

F_c is depicted graphically in Figure 3. For values of I_1 greater than L, i.e. to the left of L in Figure 3, the function F_c is unity. L is a material parameter and X is determined from Eq. 6.

The shapes of subsequent yield surfaces, defined by Eq. 9, are illustrated in Figure 4. As the yield surface hardens it traces out the locus of the shear-failure surface that is depicted in Figure 1. For a given value of I_1, the peak of each hardened surface, which represents the critical state, is well below the corresponding point on the shear-failure locus. It is this feature that permits modeling the transition from compactive to dilatant deformation that occurs before the material fails in shear.

3.1 *Constitutive Equations*

If the elastic strain is always much less than unity, the strain-rate measure can be decomposed into the sum of an elastic component and an inelastic component as

$$\dot{\varepsilon}_{ij} = \dot{\varepsilon}^e_{ij} + \dot{\varepsilon}^p_{ij} \tag{14}$$

The evaluation of the plastic strain rates follows classical plasticity theory. In the absence of evidence to the contrary, it is assumed that the yield function, f, given by Eq. 9, plays the role of a plastic potential function such that the plastic strain rates can be determined from

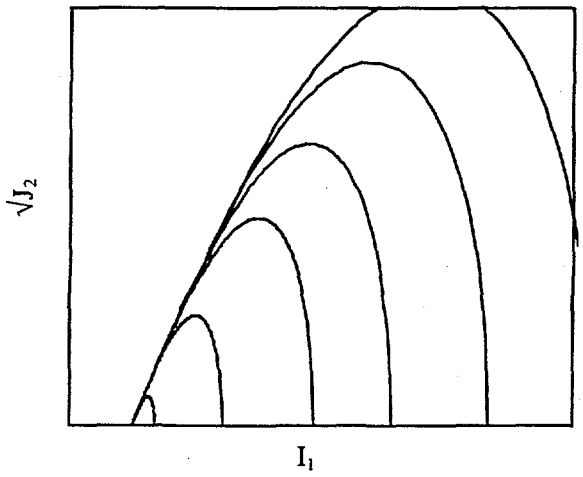

Figure 4. Nested series of continuous single-surface yield surfaces.

$$\dot{\varepsilon}^p_{ij} = \dot{\gamma}\frac{\partial f}{\partial \sigma_{ij}} \tag{15}$$

where $\dot{\gamma}$ is the consistency parameter. In this case, the flow rule is said to be associative.

The stress rate is determined from Hooke's Law with elastic strain rates derived from Eq. 14, i.e.

$$\dot{\sigma}_{ij} = C_{ijkl}\left(\dot{\varepsilon}_{kl} - \dot{\varepsilon}^p_{kl}\right) \tag{16}$$

where the fourth-order elastic coefficient matrix is given in terms of the shear modulus, G, and Poisson's ratio, ν, by

$$C_{ijkl} = 2G\left(\delta_{ik}\delta_{jl} - \frac{\nu}{1-\nu}\delta_{ij}\delta_{kl}\right) \tag{17}$$

Prager's consistency condition requires subsequent loading surfaces to pass through the loading point, i.e.

$$f(\sigma_{ij}, q) = 0 \tag{18}$$

where q are state variables governed by evolution equations of the form,

$$\dot{q} = \dot{\gamma} h_q(\sigma_{ij}, q) \tag{19}$$

in which the h_q are hardening functions. During loading, the consistency condition, Eq. 18, gives

$$\dot{f} = \frac{\partial f}{\partial \sigma_{ij}}\dot{\sigma}_{ij} + \frac{\partial f}{\partial q}\dot{q} = 0 \tag{20}$$

The consistency parameter, $\dot{\gamma}$, can then be determined as

$$\dot{\gamma} = \frac{\dfrac{\partial f}{\partial \sigma_{ij}} C_{ijkl}\dot{\varepsilon}_{kl}}{\dfrac{\partial f}{\partial \sigma_{ij}} C_{ijkl}\dfrac{\partial f}{\partial \sigma_{kl}} - \dfrac{\partial f}{\partial q}h_q} \tag{21}$$

There are two state variables, the cap hardening parameter, κ, and the shear hardening parameters, α_{ij}. Thus, the last term in the denominator of Eq. 21 becomes

$$\frac{\partial f}{\partial q}h_q = \frac{\partial f}{\partial \kappa}h_\kappa + \frac{\partial f}{\partial \alpha_{ij}}h_{\alpha_{ij}} \tag{22}$$

where the cap hardening function, h_κ, is given by

$$h_\kappa = \frac{3\dfrac{\partial f}{\partial I_1}}{\dfrac{\partial \varepsilon^p_v}{\partial X}\dfrac{\partial X}{\partial \kappa}} \tag{23}$$

If the shear hardening functions, α_{ij}, are governed by linear evolution equations,

$$\dot{\alpha}_{ij} = c^{\alpha} G^{\alpha} \dot{\varepsilon}_{ij} \quad (24)$$

where c^{α} is a material parameter and G^{α} is a scalar function, then the shear hardening functions, $h_{\alpha_{ij}}$, are given by

$$h_{\alpha_{ij}} = c^{\alpha} G^{\alpha} \left(\frac{\partial f}{\partial \sigma_{ij}} - \frac{\partial f}{\partial I_1} \delta_{ij} \right) \quad (25)$$

The scalar function, G^{α}, designed to limit the growth of the back stresses, α_{ij}, as the failure surface is approached, is given by

$$G^{\alpha} = 1 - \frac{\sqrt{\frac{1}{2} s_{ij} s_{ij}} - \sqrt{\frac{1}{2} (s_{ij} - \alpha_{ij})(s_{ij} - \alpha_{ij})}}{N} \quad (26)$$

The function $G^{\alpha} = 1$ when $\alpha_{ij} = 0$, and $G^{\alpha} \rightarrow 0$ as the stress state approaches the failure surface.

Three features are of note: (1) all subsequent loading surfaces and the initial yield surface are convex, (2) Eq. 15 implies that the plastic strain increment vector is normal to the loading surface, and (3) the plastic strain rate is linear in the stress rate. These conditions are consistent with Drucker's hypothesis for a work-hardening material, namely that useful net energy over and above the elastic energy cannot be extracted from the material, and the material is said to be stable. Thus, the development of the model to this point assumes that the material is stable. The model, therefore, may not be appropriate if the real body deforms in a non-unique manner, or can assume unstable equilibrium configurations, which may be the case for some geomaterials. If this is the case, then the model should be modified to accommodate the real behavior. One modification could be to use a non-associative flow rule and to establish the implications in terms of shear and bulk localization phenomena.

3.2 *Numerical Integration*

To solve an elasto-plastic boundary value problem, it is necessary to evaluate the plastic strain increments numerically. This requires the calculation of the incremental consistency parameter, $\Delta\gamma$. In incremental form Eq. 20 becomes,

$$\Delta\gamma = \frac{\partial f}{\partial \sigma_{ij}} \Delta\sigma_{ij} + \frac{\partial f}{\partial q} \Delta q \quad (27)$$

If equilibrium exists at the beginning of a time step, t_n, then the stresses σ_n are known and $f_n = 0$. In the simple forward scheme that will be described, all incremental quantities are approximated by the conditions at the beginning of the time step. The approximate incremental consistency condition is then given by

$$\Delta f = f_{n+1} - f_n = f\{\sigma_{ij}|_n + \Delta\sigma_{ij}, q_n + \Delta q\} - f_n = \left.\frac{\partial f}{\partial \sigma_{ij}}\right|_n \Delta\sigma_{ij} + \left.\frac{\partial f}{\partial q}\right|_n \Delta q = 0 \quad (28)$$

The approximate incremental plastic strains are given by

$$\Delta\varepsilon_{ij}^{p} \approx \Delta\gamma \left.\frac{\partial f}{\partial \sigma_{ij}}\right|_n \quad (29)$$

The approximate incremental forms of the state variables, κ and α_{ij}, are given by

$$\Delta q = \Delta\kappa|_n + \Delta\alpha_{ij}|_n \approx \Delta\gamma h_{\kappa}|_n + \Delta\gamma h_{ij}|_n \quad (30)$$

The stress increments are determined from

$$\Delta\sigma_{ij} = C_{ijkl}(\Delta\varepsilon_{kl} - \Delta\varepsilon_{kl}^{p}) \approx C_{ijkl}\left(\Delta\varepsilon_{kl} - \Delta\gamma \left.\frac{\partial f}{\partial \sigma_{kl}}\right|_n \right) \quad (31)$$

The approximate incremental consistency parameter can be determined as

$$\Delta\gamma \approx \frac{\left.\frac{\partial f}{\partial \sigma_{ij}}\right|_n C_{ijkl} \Delta\varepsilon_{kl}}{\left.\frac{\partial f}{\partial \sigma_{ij}}\right|_n C_{ijkl} \left.\frac{\partial f}{\partial \sigma_{kl}}\right|_n - \left(\left.\frac{\partial f}{\partial \kappa}\right|_n h_{\kappa}|_n + \left.\frac{\partial f}{\partial \alpha_{ij}}\right|_n h_{\alpha_{ij}}|_n \right)} \quad (32)$$

The plasticity algorithm now proceeds as follows: (1) From input total strain increments, a trial stress state is calculated as though the input total strain increment were completely elastic. The yield function is then used to determine if the trial stress state is outside the yield surface. If it is, the original stress state at the beginning of the increment is used to approximate the incremental consistency parameter from Eq. 32. (2) The approximate incremental plastic strains are then determined from Eq. 29. (3) The incremental stress increments are then determined from Eq. 31 and the updated stresses determined from

$$\sigma_{ij}|_{n+1} = \sigma_{ij}|_n + \Delta\sigma_{ij} \quad (33)$$

(4) The approximate incremental state variables are determined from Eq. 30 and the updated state variables determined from

$$q_{n+1} = q_n + \Delta q \quad (34)$$

When the plasticity algorithm is used in a finite element code, the possibility exists that the magnitude of the total strain increment passed to the material subroutine could be excessive. When this is the case, a workable solution is to use sub-incrementation of the input strain increment.

As discussed above, a key feature of the new model is the ability to model the transition from compactive to dilatant deformation that is known to occur in porous rocks well before the attainment of a peak stress. Fossum & Fredrich (2000) discuss laboratory data for two reservoir formations at the Lost Hills oil field (California) that exhibit this behavior. Baud et al. (2000) described recently laboratory rock mechanics tests performed on Solnhofen limestone that show a similar behavior.

The advantages of the continuous single-surface cap plasticity model are illustrated by comparing the predicted behavior for the traditional versus new model as applied to several data sets for a single rock. The data are from conventional triaxial compression tests, and the material is a sand unit (D) of the Upper Etchegoin Formation (late Pliocene to early Miocene). The material is a very high porosity unconsolidated diatomaceous sand with a bulk density of ~1.75 g/cc. This formation is one of the two reservoir formations at the Lost Hills oil field located in the San Joaquin basin of central California.

4.1 *Experimental procedures*

Conventional triaxial compression experiments were conducted on samples prepared from vertical cores (4½ inch diameter) recovered from the Lost Hills field. The cylindrical test specimens were prepared parallel to the core, with diameter to length dimension of 1×2 inches. Specimens were jacketed to prevent the confining fluid from penetrating the specimens and tested in a servo-controlled triaxial system with the pore pressure system drained to atmosphere. Confining pressure was measured with a conventional strain gauge transducer, and measurements of force on an internal load cell were used to calculate axial stress. Axial and radial strains were measured using cantilever-type gauges, and corrected for elastic distortion of the end-caps and jacketing material. Radial deformations were measured at two perpendicular directions along the sample mid-point, and averaged for calculation of radial strain. Load-unload cycles were performed during at least two tests to enable determination of elastic moduli.

4.2 *Traditional cap plasticity model*

Fossum & Fredrich (1998) present the determination of constitutive parameters for the traditional model for several sedimentary cycles of the Belridge Diatomite member of the Monterey Formation at the South Belridge diatomite field. Fossum & Fredrich (2000) describe the derivation of model parameters for the reservoir formations, including two sands of the Etchegoin Formation and three type diatomites

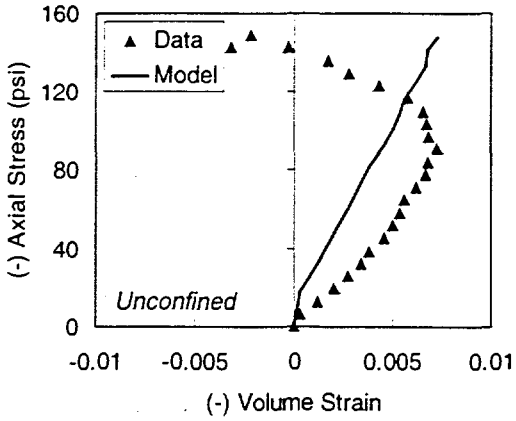

Figure 5. Measured and predicted volumetric strains as a function of axial stress in an unconfined compression test for the traditional cap plasticity model.

of the Belridge Diatomite member, at the Lost Hills field.

For the purposes of comparison, the conventional cap plasticity model is applied here to a single data set from a test conducted at atmospheric pressure. Figure 5 shows the predicted versus observed volume strains during loading. The traditional cap plasticity model cannot predict the transition from compactive to dilatant deformation that occurs before the peak stress is reached. The traditional model therefore overestimates the compactive volume strain at failure.

4.3 *Continuous, single-surface cap plasticity model*

The continuous, single-surface cap model is now applied to the suite of triaxial compression data. After the elastic moduli were estimated, the shear-failure parameters, A, B, and C (Eq. 3), were determined using nonlinear regression model fitting and the shear-failure database. The constant N defining the size of the initial shear yield surface was set to zero to permit direct comparison with the conventional cap model that has a fixed shear-failure surface. Following evaluation of elastic and shear-failure parameters, the remaining parameters were estimated through nonlinear regression involving direct simulation of the triaxial tests (Fig. 6).

In the unconfined compression test and the triaxial compression tests conducted at confining pressures of 100 and 300 psi, the volumetric strain shows compaction for a part of the test but then switches to dilatant deformation before the peak stress is attained. The triaxial compression test conducted at 1000 psi was terminated before the load path intersected the shear failure surface and prior to the possible onset of dilatancy.

Noteworthy is that the continuous, single-surface cap model predicts the transition from compactive deformation to dilatant deformation at the pre-failure stage over a significant range of confining pressures

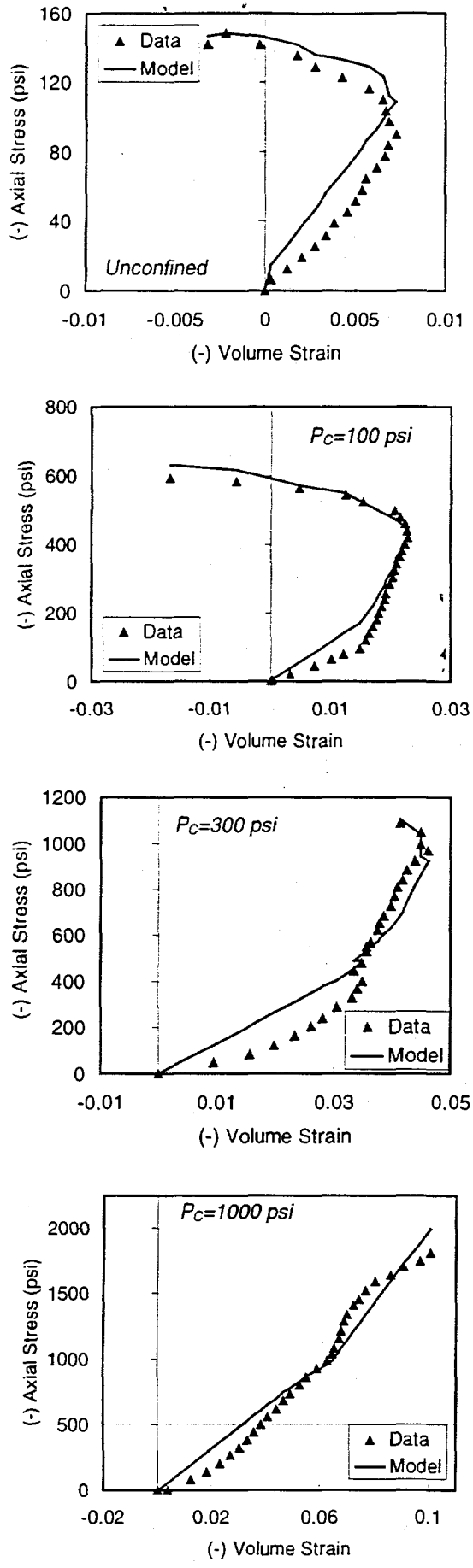

Figure 6. Measured and predicted volumetric strains as a function of axial stress for a series of triaxial compression tests for the new, continuous single-surface cap plasticity model.

without resorting to the use of a non-associative flow rule. The solution is thus stable and unique.

5 DISCUSSION

An important feature of the deformation behavior of the reservoir formation considered here is that the stress states under which the deformations are elastic are extremely limited. The initial cap is intersected almost immediately under hydrostatic compression, conventional triaxial compression, or uniaxial strain load paths. This is evident by comparing the slope of the load-unload cycles to the initial slope of the triaxial compression load path.

Figure 7 depicts the load path followed during the unconfined compression test using the traditional model. During loading, the stress point lies on the compaction yield surface until the peak stress is reached. Unless a non-associative flow rule is used, the model is incapable of predicting the dilatant volumetric strains that occur before the specimen reaches peak stress (Fig. 5). With the continuous, single-surface model (Fig. 7), the stress point can pass freely through the critical state point separating compactive from dilatant deformation during loading. The predicted volumetric strain (Fig. 6) goes from compactive to dilatant volumetric strain without the use of a non-associated flow rule.

To benchmark the performance of the new model, a large-scale three-dimensional numerical simulation was performed for direct comparison with a previ-

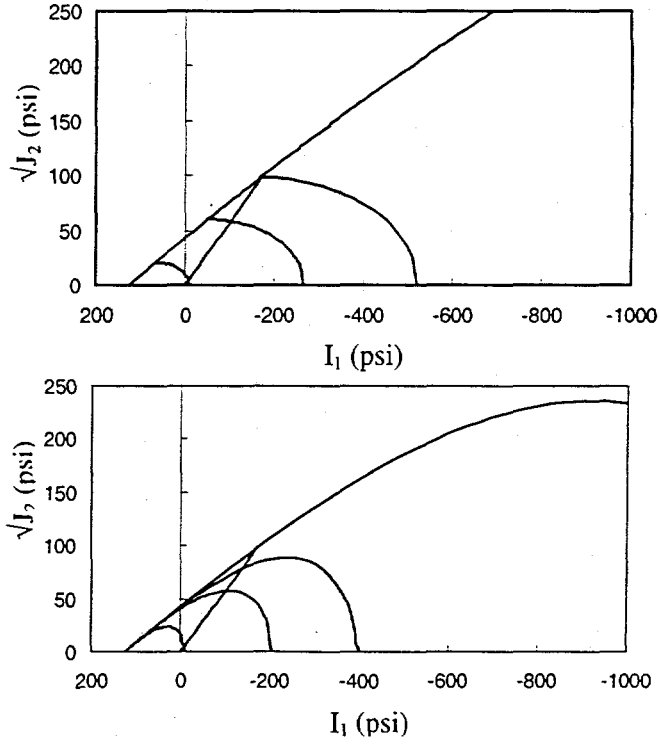

Figure 7. Load path and sequence of cap yield surfaces during the unconfined compression test for the conventional cap model (top) and new continous single-surface cap plasticity model (bottom).

ous simulation described by Fredrich et al. (1998) that used the traditional model. The computational time using the newly implemented model was ¼ that required by the traditional model.

Generally the model is capable of fitting data better than is shown here. The specific data considered here are complicated by the presence of material anisotropy. During the hydrostatic portion of the conventional triaxial compression tests, in which the three principal stresses are equal, significant anisotropy is revealed by the divergence of the radial and axial strains. Thus, the material model cannot track the axial stress versus volumetric strain as accurately as for an isotropic material. In general, the resulting difficulties in parameter estimation can be alleviated partially by use of uniaxial strain data in the fitting procedure as described by Fossum & Fredrich (2000). Under the uniaxial strain load path, the radial strain is maintained constant (equal to zero) so that the volumetric strain data is easier to fit as only one principal strain is involved. While this approach reduces the time required to iterate to an optimal parameter fit, it obviously does not eliminate the problem. Materials exhibiting significant anisotropy are better suited to a model that allows for at least transverse anisotropy. Anisotropic elastic-plastic cap models are under development currently, but they are highly complex, and challenging to implement numerically. At the current time only the isotropic model is implemented in our numerical analysis codes.

6 CONCLUSION

With the emerging capability to simulate the large-scale mechanical behavior of complex geosystems by virtue of recent advances in software and hardware, it is critical that commensurate advances are also made in material modeling capabilities for geomaterials. The continuous, single-surface cap plasticity model represents one such advance in our ability to predict accurately the behavior of complex geosystems. While fundamental material modeling assumptions can be based on the microscale physics, we have chosen instead to make assumptions about the relation between stress and strain that are physically motivated but at the phenomenological level. This approach permits, from a computational standpoint, tractable yet accurate predictions to be made on very large spatial scales.

Two key applications for this work are reservoir-scale modeling of formation compaction caused by pore pressure drawdown during oil or gas production (e.g. Fredrich et al. 1998) and field-scale modeling of the behavior of earth penetrators. For applications involving coupled processes, such as fluid flow and deformation, this work is especially significant since the ability to predict both compactive and dilatant deformation has strong impact on the evolution of fluid flow properties with inelastic deformation.

Acknowledgement. C.M. Stone contributed to the large-scale benchmark simulation using the new model. A.F.F. acknowledges support from the U.S. Department of Energy (DOE) Advanced Computational Technology Initiative. J.T.F. acknowledges support from the U.S. DOE Office of Basic Energy Sciences, Chemical Sciences, Geosciences and Biosciences Division. The laboratory testing was conducted under a collaborative National Lab – Industry project "Mitigation of well failures in diatomite reservoirs" funded by the U.S. DOE Office of Fossil Energy, Natural Gas and Oil Technology Partnership, with additional funding provided by Aera Energy LLC and Chevron USA Prod. Co. This work was performed at Sandia National Laboratories funded by the U.S. DOE under Contract No. DE-AC04-AL85000. Sandia is a multiprogram laboratory operated by Sandia Corporation, a Lockheed Martin Company, for the United States Department of Energy.

REFERENCES

Baud, P., A. Schubnel & T.-F. Wong 2000. Dilatancy, compaction and failure mode in Solnhofen limestone, submitted to *J. Geophys. Res.*

Brace, W. F., B. W. Paulding & C. H. Scholz 1966. Dilatancy in the fracture of crystalline rocks, *J. Geophys. Res.* 71: 3939-3953.

DiMaggio, F. L. & I. S. Sandler 1971. Material model for granular soils, *J. Eng. Mech. Div. ASCE* 97: 935-950.

Drucker, D. C., R. E. Gibson, and D. J. Henkel 1957. Soil mechanics and work hardening theories of plasticity, *Trans. ASCE* 122: 338-346.

Fossum, A. F. & J. T. Fredrich 1998. Estimation of constitutive parameters for the Belridge Diatomite, South Belridge Diatomite field, SAND98-1407: 32 pp. Albuquerque, New Mexico: Sandia National Laboratories.

Fossum, A. F. & J. T. Fredrich 2000. Constitutive models for the Etchegoin sands, Belridge diatomite, and overburden formations at the Lost Hills oil field, California, SAND00-xxxx: 35 pp. Albuquerque, New Mexico: Sandia National Laboratories.

Fredrich, J. T., G. L. Deitrick, J. G. Arguello & E. P. deRouffignac 1998. Reservoir compaction, surface subsidence, and casing damage: A geomechanics approach to mitigation and reservoir management, *Eurock– Rock Mechanics in Petroleum Engineering*: p. 403-412, SPE/ISRM 47284. Houston, Texas: Society of Petroleum Engineers.

Pelessone, D. 1989. A modified formulation of the cap model, Gulf Atomics Report GA-C19579 to the Defense Nuclear Agency.

Sandler, I. S. & D. Rubin 1979. An algorithm and a modular subroutine for the cap model, *Int. J. Num. Anal. Meth. Geomech.* 3: 173-186.

Schwer, L. E. & Y. D. Murry 1994. A three-invariant smooth cap model with mixed hardening, *Int. J. Num. Anal. Meth. Geomech.* 18: 657-688.

Senseny, P.E., A. F. Fossum & T. W. Pfeifle 1983. Non-associative constitutive laws for low porosity rocks, *Int. J. Num. Anal. Meth. Geomech.* 7: 101-115.